Supplementary Information for

Spontaneous magnetization of collisionless plasma

Muni Zhou, Vladimir Zhdankin, Matthew W. Kunz, Nuno F. Loureiro, and Dmitri A. Uzdensky

Muni Zhou.
E-mail: munizhou@mit.edu

This PDF file includes:

Supplementary text
Figs. S1 to S8 (not allowed for Brief Reports)
SI References

Supporting Information Text

As a supplement to the main text, we include here the detailed calculation of the Weibel instability and the validation of our analytical model described in the main text. The linear dispersion relation of the Weibel instability in the system of a driven shear flow is derived and numerically solved in Sec. 1. In Sec. 2, we present our analytical model for each stage in the non-asymptotic regime. We then test this model using kinetic particle-in-cell (PIC) simulations, whose details are provided in Sec. 3 and from which the numerical results presented in Sec. 4 are obtained.

1. Linear Weibel physics in the asymptotic regime

In this section, we calculate the dispersion relation of the Weibel modes using the unmagnetized solution of the plasma distribution function f_s [Eq. (2)]. Recall that the Weibel instability occurs at the kinetic time scale and the generated Weibel magnetic fields change the system's dynamics, the unmagnetized solution [Eq. (2)] is only valid in the short time limit $\epsilon \equiv tv_{\mathrm{th}s}/L \ll 1$. In this limit, we can take the second-order Taylor expansion of Eq. (2) for $\epsilon \equiv tv_{\mathrm{th}s}/L \ll 1$ to obtain the early-time approximation of the distribution function:

$$f_s(t,x,\boldsymbol{v}) = f_{\mathrm{M},s}\left(|\boldsymbol{v}|\right)\left\{1 + \hat{a}_0\frac{v_y}{v_{\mathrm{th}s}}\sin\left(\frac{2\pi}{L}x\right)\frac{tv_{\mathrm{th}s}}{L} - \frac{1}{2}\left[2\pi\hat{a}_0\frac{v_xv_y}{v_{\mathrm{th}s}^2}\cos\left(\frac{2\pi}{L}x\right) + \hat{a}_0^2\left(1-\frac{v_y^2}{v_{\mathrm{th}s}^2}\right)\sin^2\left(\frac{2\pi}{L}x\right)\right]\left(\frac{tv_{\mathrm{th}s}}{L}\right)^2\right\} + \mathcal{O}(\epsilon^3). \quad \text{[S1]}$$

We first show that Eq. (S1) is a multivariate distribution function under certain approximations, and can thus be written as a tri-Maxwellian in an orthonormal coordinate system (Sec. 1A). We then numerically solve the dispersion relation for an oblique Weibel mode in a tri-Maxwellian plasma and find the dependence of the growth rate of the most unstable mode, γ_{w}, on the thermal pressure anisotropy, Δ (Sec. 1B) .

A. Coordinate transformation of f_s. Let us specify a location $x = 0$ at which maximum shear occurs and thereby remove the spatial dependence of f_s. The plasma at this position undergoes the strongest phase mixing, and thus has the maximum thermal pressure anisotropy. The dynamics of the Weibel instability at this position is therefore representative of that in the whole system. In the small-time limit $\epsilon \equiv tv_{\mathrm{th}s}/L \ll 1$ and at $x = 0$, Eq. (2) becomes

$$\begin{aligned}\widetilde{v}_y &\equiv v_y + \frac{La_0}{2\pi v_x}\left[1-\cos\left(\frac{2\pi}{L}v_xt\right)\right]\\ &\simeq v_y + \hat{a}_0\pi v_x\left(\frac{tv_{\mathrm{th}s}}{L}\right)^2 + \mathcal{O}(\epsilon^3).\end{aligned} \quad \text{[S2]}$$

Combining the time evolution of thermal pressure anisotropy [Eq. (4)],

$$\Delta_s(t, x=0) = \frac{3}{2}\pi\hat{a}_0\left(\frac{tv_{\mathrm{th}s}}{L}\right)^2 + \mathcal{O}(\epsilon^3), \quad \text{[S3]}$$

we can simplify the expression of $\widetilde{v}_y$ as

$$\widetilde{v}_y \equiv v_y + \frac{2}{3}\Delta_s(t)v_x, \quad \text{[S4]}$$

and that of f_s at $x = 0$ as

$$f_s(\boldsymbol{v}) = F_{\mathrm{M},s}\left[\left(1+\frac{4}{9}\Delta_s^2\right)v_x^2 + \frac{4}{3}\Delta_sv_xv_y + v_y^2 + v_z^2\right]. \quad \text{[S5]}$$

In this case, f_s possesses the form of a multivariate normal distribution and can thus be transformed to an orthonormal coordinate basis $\{v_{x'}, v_{y'}, v_z\}$ and written as the tri-Maxwellian distribution

$$\widetilde{f}_s \propto \exp\left[-\left(\frac{v_{x'}^2}{2T_{x',s}} + \frac{v_{y'}^2}{2T_{y',s}} + \frac{v_z^2}{2T_{z,s}}\right)\right]. \quad \text{[S6]}$$

Here $T_{x',s}$, $T_{y',s}$, and $T_{z,s}$, with $T_{y',s} > T_{z,s} > T_{x',s}$, are the eigenvalues of the covariance matrix of f_s, and $v_{x'}$, $v_{y'}$, and v_z are the corresponding eigenvectors. Note that the orientation of the orthonormal coordinate evolves with time. The thermal pressure anisotropy (defined in the Theory section in the main text) thus becomes $\Delta_s \equiv \sqrt{\langle(P_{\max,s}/P_{\perp,s})^2\rangle} - 1 = \sqrt{\langle(T_{y',s}/T_{\perp,s})^2\rangle} - 1$, where $T_{\perp,s} = (T_{x',s} + T_{z,s})/2$.

B. General dispersion relation for Weibel instability. We proceed to derive the linear dispersion relation of the oblique Weibel modes for a tri-Maxwellian distribution function. The goal of this calculation is to obtain the dependence on pressure anisotropy of the growth rate of the most unstable Weibel mode. For simplicity, we consider a system that is 3D in velocity space ($v_{x'}$,$v_{y'}$,v_z) and 2D in configuration space (x',y'). Our numerical results in Sec. 4 show that, at least for the unmagnetized stage and the linear Weibel stage, systems with 3D and 2D configuration space exhibit almost identical results, thereby justifying this approximation.

We begin by considering the tri-Maxwellian initial distribution

$$\widetilde{f}_{0,s}(v_{x'}, v_{y'}, v_z) = \widetilde{f}_{0x',s}(v_{x'})\widetilde{f}_{0y',s}(v_{y'})\widetilde{f}_{0z,s}(v_z), \quad \text{[S7]}$$

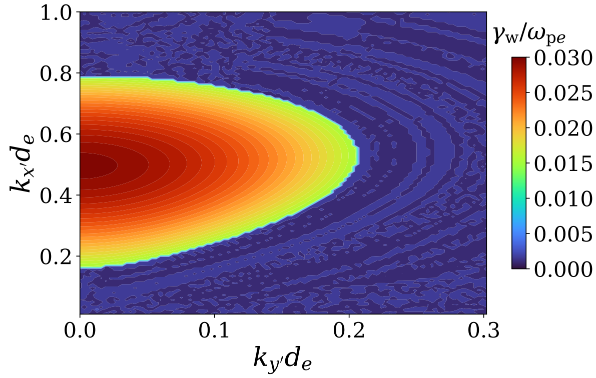

Fig. S1. Two-dimensional spectrum of the normalized growth rate of the Weibel modes, $\gamma_{\rm w}/\omega_{\rm pe}$, in terms of $k_{x'}d_e$ and $k_{y'}d_e$ for $\Delta_e = 0.4$. The most unstable mode is the purely transverse mode ($k_{y'}d_e = 0$).

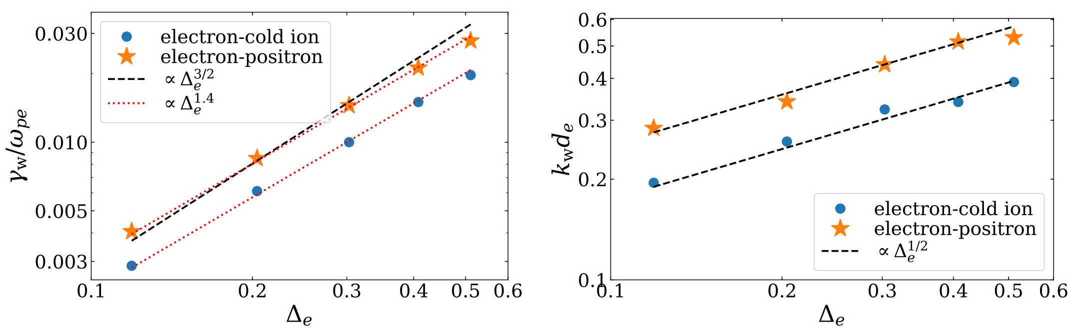

Fig. S2. Numerical solution of the Weibel dispersion relation. Left: Maximum normalized Weibel growth rate, $\gamma_{\rm w}/\omega_{\rm pe}$, versus the thermal pressure anisotropy. The scalings $\gamma_{\rm w}/\omega_{\rm pe} \sim \Delta_{\rm e}^{3/2}$ and $\gamma_{\rm w}/\omega_{\rm pe} \sim \Delta_{\rm e}^{1.4}$ are shown for reference. Right: Normalized wavenumber of the most unstable Weibel mode, $k_{\rm w}d_e$, versus the thermal pressure anisotropy. A $\gamma_{\rm w}/\omega_{\rm pe} \sim \Delta_{\rm e}^{1/2}$ scaling is shown for reference.

where

$$\widetilde{f}_{0a,s}(v_a) = \frac{1}{\sqrt{\pi}v_{{\rm th}a,s}} \exp\left\{-\frac{v_a^2}{2v_{{\rm th}a,s}^2}\right\}, \tag{S8}$$

$v_{{\rm th}a,s} \equiv \sqrt{T_{a,s}/m_s}$, and $a \in \{x', y', z\}$. To this distribution we add a linear perturbation, whose 2D spatial dependence is characterized by a wavenumber that contains both transverse and longitudinal components:

$$\boldsymbol{k} = k_{x'}\hat{\boldsymbol{x}}' + k_{y'}\hat{\boldsymbol{y}}'. \tag{S9}$$

The general expression for the components of the dielectric tensor, which specifies the oscillatory response of the plasma, is

$$\epsilon_{ab}(\omega, \mathbf{k}) = \left(1 - \sum_s \frac{\omega_{\rm ps}^2}{\omega^2}\right)\delta_{ab} + \sum_s \frac{\omega_{\rm ps}^2}{\omega^2}\int {\rm d}^3\boldsymbol{v}\ \frac{v_a v_b}{\omega - \boldsymbol{k}\cdot\boldsymbol{v}}\,\boldsymbol{k}\cdot\frac{\partial \widetilde{f}_{0,s}}{\partial \boldsymbol{v}}, \tag{S10}$$

where ω is the (complex) frequency of the response. The components of the associated dispersion matrix are given by

$$D_{ab}(\omega, \boldsymbol{k}) = \epsilon_{ab} + \frac{k_a k_b}{\omega^2}c^2 - \frac{k^2c^2}{\omega^2}\delta_{ab}, \tag{S11}$$

where $k = |\boldsymbol{k}|$. Plugging in the tri-Maxwellian distribution function $\widetilde{f}_{0,s}$ [Eq. (S7)] and defining the variables $\xi \equiv (\omega - k_{y'}v_{y'})/|k_{x'}|v_{{\rm th}x'}$, $u \equiv v_{x'}/v_{{\rm th}x'}$, and $\mathcal{Z}(\xi) \equiv \pi^{-1/2}\int {\rm d}u\, \exp(-u^2)(u-\xi)^{-1}$, we obtain

$$D_{y'y'} = 1 - \frac{k_{x'}^2c^2}{\omega^2} + \sum_s \frac{\omega_{\rm ps}^2}{\omega^2}\left\{-1 + \frac{T_{y'}}{T_{x'}} + \frac{k_{y'}}{k_{x'}}\frac{v_{{\rm th}y'}}{v_{{\rm th}x'}}\int {\rm d}v_{y'}\,\frac{v_{y'}^3}{v_{{\rm th}y'}^3}\widetilde{f}_{y'}\mathcal{Z}(\xi) + 2\frac{v_{{\rm th}y'}^2}{v_{{\rm th}x'}^2}\int {\rm d}v_{y'}\,\frac{v_{y'}^2}{v_{{\rm th}y'}^2}\widetilde{f}_{y'}\xi\mathcal{Z}(\xi)\right\}, \tag{S12}$$

$$D_{y'x'} = D_{x'y'} = \frac{k_{y'}k_{x'}c^2}{\omega^2} + \sum_s \frac{\omega_{\rm ps}^2}{\omega^2}\left\{\frac{k_{y'}}{k_{x'}} + \frac{k_{y'}}{k_{x'}}\int {\rm d}v_{y'}\,\frac{v_{y'}^2}{v_{{\rm th}y'}^2}\widetilde{f}_{y'}\xi\mathcal{Z}(\xi) + 2\frac{v_{{\rm th}y'}}{v_{{\rm th}x'}}\int {\rm d}v_{y'}\,\frac{v_{y'}}{v_{{\rm th}x'}}\widetilde{f}_{y'}\xi\left[1 + \xi\mathcal{Z}(\xi)\right]\right\}, \tag{S13}$$

and

$$D_{x'x'} = 1 - \frac{k_{y'}^2 c^2}{\omega^2} + \sum_s \frac{\omega_{\rm ps}^2}{\omega^2} \times \left\{ \frac{k_{y'}}{k_{x'}} \frac{v_{\rm thx'}}{v_{\rm thy'}} \int \mathrm{d}v_{y'}\, \frac{v_{y'}}{v_{\rm thy'}} \widetilde{f}_{y'} \xi \left[1 + \xi \mathcal{Z}(\xi)\right] + 2 \int \mathrm{d}v_{y'}\, \widetilde{f}_{y'} \xi^2 \left[1 + \xi \mathcal{Z}(\xi)\right] \right\}. \tag{S14}$$

The nontrivial solution of the mode's dispersion relation is given by

$$\det \mathbf{D} = 0 \implies D_{y'y'} D_{x'x'} - D_{y'x'} D_{x'y'} = 0. \tag{S15}$$

We numerically solve Eq. (S15) for two systems: (i) an electron-positron plasma in which both species respond to the electromagnetic fluctuations and $\Delta_e = \Delta_p$; and (ii) an electron-ion (proton) plasma where only electrons contribute to the Weibel modes and ions are considered as a cold and immobile neutralizing background. For a given thermal pressure anisotropy Δ_e, we scan across all $\boldsymbol{k}$ to obtain the 2D spectrum of the Weibel growth rate in terms of $k_{x'} d_e$ and $k_{y'} d_e$. Fig. S1 shows an example for a given $\Delta_e = 0.4$ (the value of anisotropy that a system with $\hat{a_0} = 0.2\pi^2$ reaches at $\tau_{\rm lin}$). We find the mode with the largest growth rate $\gamma_{\rm w}$ at the corresponding wavenumber $k_{\rm w}$. The dependence of $\gamma_{\rm w}$ and $k_{\rm w}$ on Δ_e is shown in Fig. S2. The canonical scaling laws $\gamma_{\rm w}/\omega_{\rm pe} \sim \Delta_e^{3/2}$ and $k_{\rm w} d_e \sim \Delta_e^{1/2}$ (1) agree well for both a electron-positron plasma and an electron-cold ion plasma.

In addition, we found that the most unstable mode is always the purely transverse mode (i.e., $k_{y'} = 0$). This suggests that Weibel instability is the primary instability in the configuration of a driven shear flow at $t v_{\rm th}/L \ll 1$. Other instabilities, such as the electrostatic two-stream instability, do not play a significant role in the system we consider. This conclusion might be different for other configurations. For example, for a system of counter-streaming flows, the dominant instability can be the two-stream instability (especially in the non-relativistic regime), depending on the ratio of flow to thermal velocity (2).

Note that the Weibel growth rate and wavenumber obtained from the dispersion relation Eq. (S15) based on the distribution function in Eq. (S6), valid in the small $t v_{\rm th}/L$ limit, is considered as the asymptotic solution. We expect this solution to apply when the system possesses an asymptotically large scale separation L/d_e.

2. Analytical model in non-asymptotic regimes

In the main text, we present the analytical model in the asymptotic regime ($L/d_e \gg 1$), where predictive scalings can be made for the saturated magnetic energy ($\propto \beta_{e,\rm sat}^{-1}$) and the length scale of magnetic fields ($\propto k_{\rm w} d_e$). However, for systems lacking such a scale separation (such as those achievable in numerical simulations and laboratory laser experiments), at the moment when the Weibel magnetic fields are rapidly growing, f_s already deviates significantly from a (tri-)Maxwellian distribution and possesses a complex form. In this case, the early-time behavior for Δ_e [Eq. (4)] is no longer a good approximation, and a different Weibel dispersion relation (different dependence of γ_B and $k_{\rm w}$ on Δ_e) is expected. Due to the lack of explicit analytical expressions for Δ_e, γ_B, and $k_{\rm w}$ in the non-asymptotic regime, free parameters are used in the model and are to be determined by first-principles numerical simulations. In this section, we follow the theoretical framework described in the Theory section in the main text and derive the model in the non-asymptotic regime.

A. Linear Weibel stage. In this stage, we assume that the dependence of the growth rate of the magnetic field, γ_B, on Δ_e remains a power law, and the power-law exponent is set to be a free parameter α:

$$\gamma_B \equiv \frac{\mathrm{d} \ln B}{\mathrm{d}t} \sim \Delta_e^{\alpha} \omega_{\rm pe} \frac{v_{\rm the}}{c}. \tag{S16}$$

In the asymptotic regime, we expect $\alpha = 3/2$. During the linear stage of the Weibel instability, the magnetic field is not yet strong enough to affect the background accelerating plasma flow. The system should thus follow the unmagnetized solution [Eq. (2)], based on which the evolution of Δ_e at arbitrary times does not have an explicit analytical expression. For simplicity, we assume a power-law scaling

$$\Delta_e \sim \hat{a}_0 (t v_{\rm the}/L)^{\kappa}, \tag{S17}$$

where $\kappa = 2$ in the asymptotic regime [Eq. (4)].

As we discuss in the main text, if the time scale for the growth of magnetic fields is well separated from that of Δ_e, *viz.* $\gamma_B \gg \partial_t \Delta_e / \Delta_e \sim \partial_t \gamma_B / \gamma_B$, we can integrate Eq. (S16) to obtain the evolution of the magnetic field. Assuming a constant mean thermal pressure of the system, the time evolution of β_e^{-1} (representing magnetic energy) can then be written as

$$\beta_e^{-1} \simeq \beta_0^{-1} \exp\left[\frac{2\hat{a}_0^{\alpha}}{\kappa\alpha + 1} \left(\frac{t v_{\rm the}}{L} \right)^{\kappa\alpha+1} \frac{L}{d_e} \right], \tag{S18}$$

where β_0^{-1} is determined by the initial magnetic-field perturbation at $k_{\rm w}$.

Eq. (S18) is expected to be valid until the end of the linear electron Weibel phase ($\tau_{\rm lin}$), when the argument in the exponential function in Eq. (S18) is expected to reach order unity, resulting in the scaling

$$\tau_{\rm lin} \sim \left(\frac{L}{d_e} \right)^{-1/(\kappa\alpha+1)} \hat{a}_0^{-\alpha/(\kappa\alpha+1)}. \tag{S19}$$

It follows that the electron pressure anisotropy Δ_e and the magnetic growth rate γ_B at $\tau_{\rm lin}$ should satisfy

$$\Delta_e(\tau_{\rm lin}) \sim \left(\frac{L}{d_e}\right)^{-\kappa/(\kappa\alpha+1)} \hat{a}_0^{1/(\kappa\alpha+1)}, \quad \text{[S20]}$$

$$\frac{\gamma_B(\tau_{\rm lin})}{\omega_{\rm pe}} \sim \left(\frac{L}{d_e}\right)^{-\kappa\alpha/(\kappa\alpha+1)} \hat{a}_0^{\alpha/(\kappa\alpha+1)} \frac{v_{\rm the}}{c}. \quad \text{[S21]}$$

B. Saturation of Weibel instability. As we explain in the main text, the length scale of the Weibel seed fields do not change significantly during the nonlinear Weibel stage before its saturation. The dependence of the length scale of the Weibel magnetic field, $k_{\rm w}^{-1}(\tau_{\rm lin})$, on $\Delta_e(\tau_{\rm lin})$ is determined by the linear dispersion relation of the Weibel instability. Alongside the power-law dependence of γ_B on Δ_e [Eq. (S16)], we also assume a power-law dependence of $k_{\rm w}$ on Δ_e:

$$k_{\rm w} \simeq \Delta_e^{\nu}/d_e, \quad \text{[S22]}$$

where we expect $\nu = 1/2$ in the asymptotic regime. It follows from Eq. (S20) that the dependence of $k_{\rm w}d_e$ on L/d_e and $\hat{a}_0$ satisfies

$$k_{\rm w}d_e \sim \left(\frac{L}{d_e}\right)^{-\kappa\nu/(\kappa\alpha+1)} \hat{a}_0^{\nu/(\kappa\alpha+1)}. \quad \text{[S23]}$$

The average electron Larmor radius can be estimated as $\rho_e \simeq \beta_e^{1/2} d_e$. Combining this relation with Eq. (S22), the trapping condition, $k_{\rm w}\rho_e \sim 1$, provides the estimate of the value of β_e^{-1} at saturation:

$$\beta_{e,\rm sat}^{-1} \sim \Delta_e^{2\nu}(\tau_{\rm lin}). \quad \text{[S24]}$$

Combined with Eq. (S20), we obtain the dependence of the saturated β_e^{-1} on the system parameters:

$$\beta_{e,\rm sat}^{-1} \sim \left(\frac{L}{d_e}\right)^{-\frac{2\nu\kappa}{\kappa\alpha+1}} \hat{a}_0^{\frac{2\nu}{\kappa\alpha+1}}. \quad \text{[S25]}$$

Eq. (S23) and Eq. (S25) provide the main deliverable of our model–the scaling dependence of the length scale $[\propto(k_{\rm w}d_e)^{-1}]$ and amplitude $(\propto\beta_{e,\rm sat}^{-1})$ of the saturated seed magnetic fields on the two key dimensionless parameters: $\hat{a}_0$ and L/d_e. Setting L/d_e as a parameter allows us to test the predicted scalings [Eq. (S21)–Eq. (S25)] using numerical simulations with relatively small values of L/d_e, and then extrapolate to relevant astrophysical systems with asymptotically large L/d_e. Note that another fundamental quantity in astrophysical environments—the normalized temperature $\theta_s \equiv T_s/m_s c^2$—is not a critical parameter for this problem since we focus only on the sub-relativistic regime. The Weibel magnetic energy and the thermal pressure are both proportional to θ_s. Therefore, the saturated β_e^{-1}, reflecting the level of magnetization that can be achieved through the Weibel instability, is not a function of temperature (at fixed $\hat{a}_0$).

Our model is predictive for the scaling dependence of the dominant wavenumber and inverse beta for the saturated fields in the asymptotic regime: $k_{\rm w}d_e \sim (L/d_e)^{-1/4}\hat{a}_0^{1/8}$ and $\beta_{e,\rm sat}^{-1} \sim (L/d_e)^{-1/2}\hat{a}_0^{1/4}$ (shown in the main text). In regimes lacking a large enough scale separation L/d_e, we have to set the exponents (α, κ, and ν) of certain power-law dependencies [Eq. (S16)–Eq. (S17) and Eq. (S22)] as undetermined parameters. Those exponents are to be determined by the first-principles numerical simulations discussed in Sec. 4. However, the derived scalings based on these undetermined exponents [Eq. (S19)–Eq. (S21), Eq. (S23)–Eq. (S25)] will be tested independently using the numerical results to validate the model.

3. Simulation setup

To test and calibrate our model in the non-asymptotic regimes, we perform the first-principles PIC simulations using the code ZELTRON (3) of an initially unmagnetized plasma driven by an external shearing force. The detailed setup is described in the Numerical Experiment section in the main text. The system is intrinsically multi-scale, containing the macroscopic, slow, fluid-scale dynamics driven by the external shear force; and the fast, kinetic-scale dynamics of plasma instabilities. In order to explore both the slow and fast dynamics, we perform parameter scans on the two key parameters: S_0 and L/d_e. Both 3D and 2D runs are performed with the same setup, with the 2D runs resolving only the x-y plane (but including all three velocity components). The main purpose of the 2D runs is to achieve the largest values of L/d_e that we can afford, and thus a better separation between the macro- and microscopic dynamics. The dynamics in the unmagnetized stage is identical between 2D and 3D systems, and we expect their Weibel physics to be qualitatively similar—the scaling laws [Eq. (S16)–Eq. (S25)] hold for both 2D and 3D cases with only a constant factor difference. On the other hand, the 2D runs do not capture possible dynamics in the z direction such as the kink instability and the coalescence of Weibel filaments. However, we will find (in Sec. 4) that those dynamics only affect the long-term evolution of Weibel filaments and do not change the main deliverable of this study: the scaling dependence of saturated Weibel seed fields on L/d_e and S_0.

We conduct scans in S_0 and L/d_e. For the scan in S_0, which we vary across $S_0 \in \{0.1, 0.2, 0.3, 0.4\}$, we perform one group of 3D runs with fixed $L/d_e = 32$, and two groups of 2D runs with fixed $L/d_e = 512$ and $L/d_e = 1024$, respectively. For the scan in L/d_e, we perform a group of 3D runs with fixed $S_0 = 0.2$ and varying $L/d_e \in \{32, 48, 64, 96, 128, 192\}$, and a group of 2D runs with fixed $S_0 = 0.2$ and varying $L/d_e \in \{32, 48, 64, 96, 128, 192, 256, 384, 512, 769, 1024\}$. For all simulations, the (initial)

Debye length $\lambda_{\mathrm{De}} = \Delta x$ where Δx is the cell length, and $d_e = 4\Delta x$ (so that $d_e/\lambda_{\mathrm{De}} = \sqrt{1/\theta_e} = 4$). All 2D runs are performed using 256 particles per cell (PPC) (128 per species). The 3D runs with fixed $S_0 = 0.2$ and varying L/d_e are performed with 32 PPC, and those with fixed $L/d_e = 32$ and varying S_0 have 256 PPC (for which the results are similar to those in runs with 32 PPC with all the other parameters kept identical). All runs are evolved for more than one thermal crossing time to include both the micro- and macroscopic dynamics.

For the scan in S_0, the scale separation L/d_e is fixed. We vary the amplitude of the forcing to the system and study how the kinetic physics responds to it. For the scan in L/d_e, the system size L is kept fixed and d_e is varied by changing the plasma density. In other words, we drive the fluid-scale dynamics identically and study how the system's kinetic-scale response changes with scale separation.

4. Numerical results — Quantitative scalings from parameter scans.

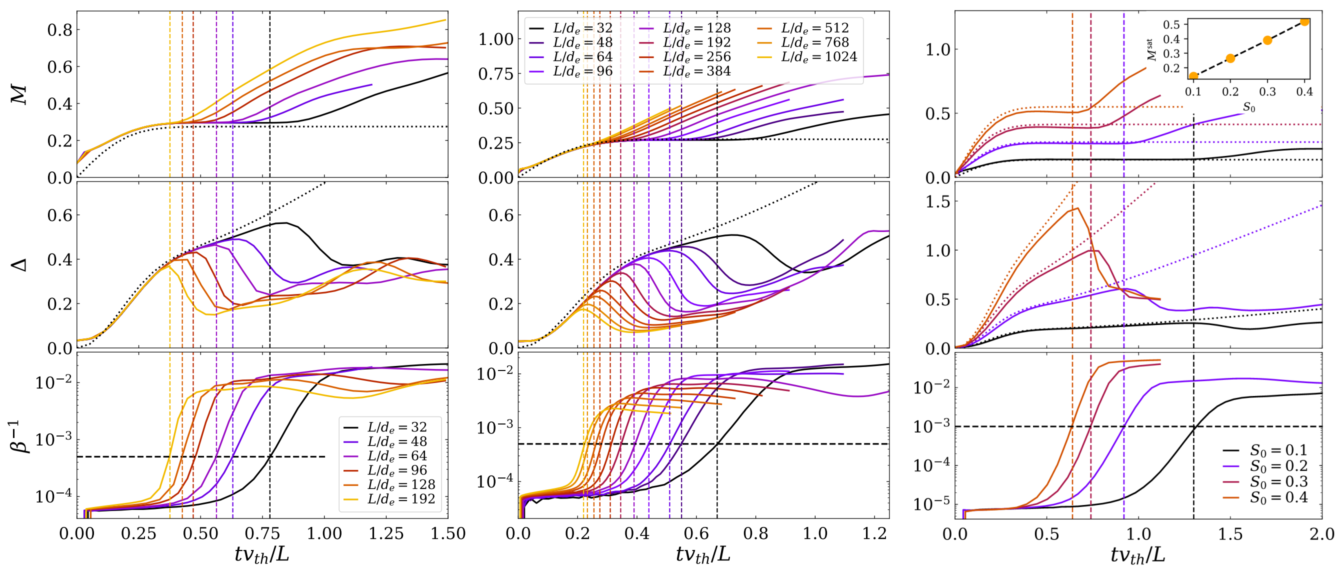

Fig. S3. Time evolution of M (top row), Δ (middle row), and β^{-1} (bottom row). Left: 3D runs with varying L/d_e and fixed $S_0 = 0.2$. Middle: 2D runs with varying L/d_e and fixed $S_0 = 0.2$. Right: 3D runs with varying S_0 and fixed $L/d_e = 32$. Vertical dashed lines indicate $tv_{\mathrm{th}}/L = \tau_{\mathrm{lin}}$ for corresponding runs. Horizontal dashed lines in the bottom panels of each column indicate the values of β^{-1} at τ_{lin}. The dotted lines in the top and middle panels are the analytical solutions for M and Δ, respectively. The inset figure in the top-right panel shows the values of M at the plateau versus S_0.

In the main text, we focus on analyzing a fiducial case and show its qualitatively agreement with our model. In this SI, we focus on the parameter scans (in S_0 and L/d_e), analyzing the scaling laws of key quantities (Δ, β^{-1}, and γ_B) at critical moments of time (τ_{lin} and τ_{sat}) and comparing our numerical results with the predictions derived in Sec. 2 [Eq. (S19)–Eq. (S21) and Eq. (S24)–Eq. (S25)].

The time evolution of M, Δ, and β^{-1} for these two parameter scans is shown in Fig. S3. For runs performed at fixed S_0, during the unmagnetized and linear Weibel stages for each run, the evolution of macroscopic quantities (M and Δ) is identical (left and middle columns in Fig. S3). For runs with varying S_0 (right column in Fig. S3), $M(t)$ and $\Delta(t)$ evolve differently, following Eq. (1). Simulations with different L/d_e and S_0 enter the exponential magnetic-field growth stage at different moments of time. Even for systems sharing the same background evolution of $M(t)$ and $\Delta(t)$, their increase of β^{-1} differs (left and middle column). Systems with larger L/d_e have a shorter kinetic time scale $\omega_{\mathrm{p}}^{-1} = d_e/c$ (relative to the macroscopic time scale L/v_{th}) and thus a faster increase of β^{-1} given that the growth rate of the Weibel instability $\gamma_B \propto \omega_{\mathrm{p}}$. Before entering the nonlinear Weibel stage, the magnetic-field strength is not yet significant enough to affect the macroscopic background evolution and, therefore, M and Δ have not deviated from the unmagnetized solution (dotted lines).

In the Theory section in the main text, we predict that, in an unmagnetized plasma, the bulk flow velocity, and thus M, should reach a saturation stage due to the developed effective viscous force that balances the external forcing. In our numerical results, this feature is indeed observed for runs with $L/d_e \lesssim 200$. The force balance condition [Eq. (5)] provides an estimate of the plateau level $M^{\mathrm{sat}} \propto S_0$ [Eq. (6)]; this scaling is confirmed by the numerical results shown in the inset figure in the right column of Fig. S3. For runs with $L/d_e \gtrsim 200$, the plateau of M does not have enough time to develop because the overall dynamics is changed by the Weibel magnetic field before the force balance is reached.

In our simulations with fixed $S_0 = 0.2$, two regimes exist, depending on the scale separation L/d_e. For $L/d_e \lesssim 200$, the linear Weibel stage that occurs around τ_{lin} is reached after τ_0, the moment when the unmagnetized plasma reaches a steady-state flow and M reaches the plateau. We call this the post-plateau regime. For $L/d_e \gtrsim 200$, τ_{lin} is reached before τ_0. Weibel fields grow shortly after the system is driven and change the overall dynamics before the steady-state flow could occur. We call this the pre-plateau regime. We denote by $(L/d_e)_{\mathrm{cr}}$ the critical scale separation where the transition between the preand post-plateau regimes occurs. Near this transition, the Weibel fields grow rapidly while the flow approaches the steady state, i.e., $\tau_0 \approx \tau_{\rm lin}$. Combined with the estimation of these two times: $\tau_0 \sim 1/2\pi$ (see Theory section in the main text) and $\tau_{\rm lin} \sim (L/d_e)^{-1/(\kappa\alpha+1)} S_0^{-\alpha/(\kappa\alpha+1)}$ [Eq. (S19)], we obtain the dependence of this critical scale separation on the drive of the system: $(L/d_e)_{\rm cr} \propto S_0^{-\alpha}$.

Most of our 3D simulations are in the post-plateau regime, with the largest ones ($L/d_e = 128, 192$) marginally entering the pre-plateau regime, while our 2D runs, where much larger values of L/d_e can be afforded, allow us to explore the pre-plateau regime. The pre-plateau regime is closer to the asymptotic regime, which is relevant to astrophysical systems where L/d_e is typically an asymptotically large number. In the following subsections, we discuss the scaling laws measured during the the linear stage and saturation of the Weibel instability for both the pre- and post-plateau regimes.

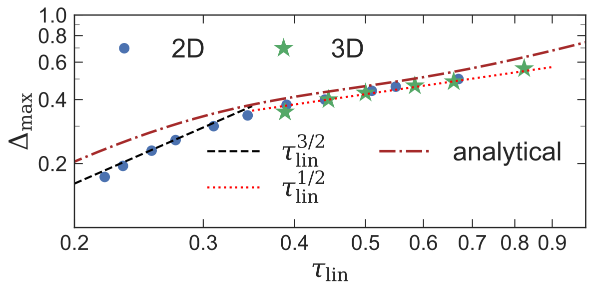

Fig. S4. Results of $\Delta_{\rm max}$ versus $\tau_{\rm lin}$ from 2D and 3D runs with varying L/d_e and fixed $S_0 = 0.2$. The dash-dotted curve shows the pressure anisotropy Δ as a function of time calculated from the analytical solution Eq. (2). Red-dotted and black-dashed lines show power-law fits to the post-plateau and pre-plateau regimes, respectively.

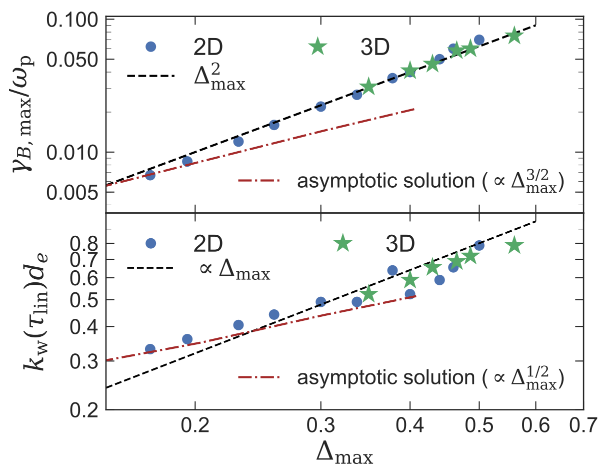

Fig. S5. Weibel growth rate and wavenumber from 2D and 3D runs with varying L/d_e and fixed $S_0 = 0.2$. Top: $\gamma_{B,\rm max}/\omega_{\rm p}$ versus $\Delta_{\rm max}$. The dashed line shows the $\sim \Delta_{\rm max}^2$ fit. Bottom: $k_{\rm w}(\tau_{\rm lin})d_e$ versus $\Delta_{\rm max}$. The black dashed line shows a reference linear scaling. The brown dash-dotted lines show the asymptotic solution of the linear growth rate of the most unstable Weibel mode (top) and its corresponding wavenumber (bottom) as a function of pressure anisotropy. The values of measured growth rate and wavenumber from the two runs with the largest L/d_e (the two left-most data points) agree with the asymptotic solution.

A. Scaling laws at the end of linear Weibel stage. In the linear Weibel stage, the plasma is unmagnetized and Δ increases due to the external forcing until reaching its maximum value $\Delta_{\rm max}$ at $\tau_{\rm lin}$, whereupon the effects of magnetic fields become important. For runs with varying L/d_e, and thus varying $\tau_{\rm lin}$, the measured $\Delta_{\rm max}$ as a function of $\tau_{\rm lin}$ follows the time evolution of Δ calculated with the unmagnetized analytical solution Eq. (2), as is shown in Fig. S4. The time evolution of Δ, and thus the dependence of $\Delta_{\rm max}$ on $\tau_{\rm lin}$, can be approximated with power-law expressions within certain ranges of time: $\Delta \simeq \hat{a}_0(tv_{\rm th}/L)^\kappa$ with $\hat{a}_0 \propto S_0$ [Eq. (S17)]. In our runs, $\kappa = 1/2$ is measured for the post-plateau regime (small L/d_e, large $\tau_{\rm lin}$), and $\kappa = 3/2$ for the pre-plateau regime (large L/d_e, small $\tau_{\rm lin}$). In the asymptotic regime, we expect the scaling $\kappa = 2$ based on the expansion of the analytical solution at asymptotically small $tv_{\rm th}/L$ [Eq. (4)].

The growth rate of the most unstable mode and its wavenumber in the linear Weibel stage is expected to have power-law dependencies on anisotropy: $\gamma_B \simeq \Delta^\alpha \omega_{\rm p} v_{\rm th}/c$ [Eq. (S16)] and $k_{\rm w} d_e \simeq \Delta^\nu$ [Eq. (S22)]. Fig. S5 shows the measured magnetic growth rate at $\tau_{\rm lin}$, $\gamma_{B,\rm max}$, (top panel) and the normalized wavenumber, $k_{\rm w} d_e$, corresponding to the peak of the isotropic magnetic power spectrum $M(k)$ at $\tau_{\rm lin}$ (bottom panel), as functions of measured $\Delta_{\rm max}$ for runs with varying L/d_e. The $\gamma_{B,\rm max}/\omega_{\rm p} \propto \Delta_{\rm max}^2$ (i.e., $\alpha = 2$) and $k_{\rm w} d_e \propto \Delta_{\rm max}$ (i.e., $\nu = 1$) scalings are found across most of the values of L/d_e, except for

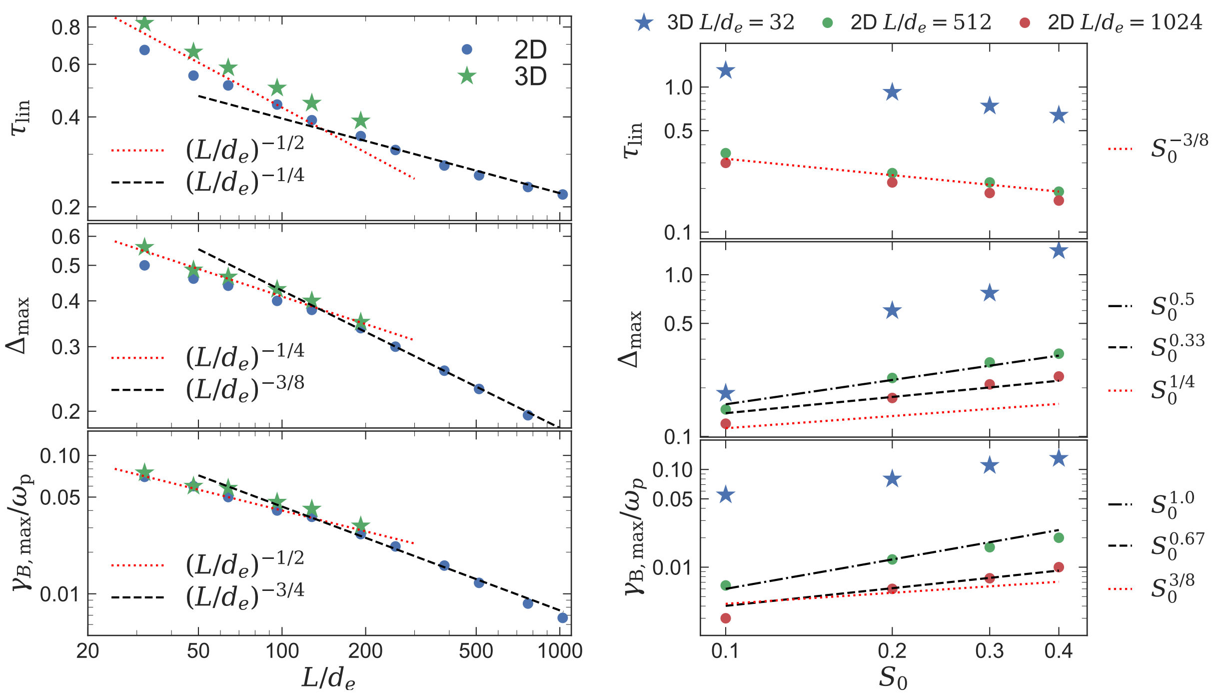

Fig. S6. Right: Plots of $\tau_{\rm lin}$ (top), $\Delta_{\rm max}$ (middle), and $\gamma_{B,\rm max}/\omega_{\rm p}$ (bottom) versus L/d_e for 2D and 3D runs with varying L/d_e and fixed $S_0 = 0.2$. Red (black) dotted lines show the predicted scalings in post-plateau (pre-plateau) regime. Left: Plots of $\tau_{\rm lin}$ (top), $\Delta_{\rm max}$ (middle), and $\gamma_{B,\rm max}/\omega_{\rm p}$ (bottom) versus S_0 for 2D and 3D runs with varying S_0. Red dotted lines show the theoretical predictions and black dashed lines show fits to the data points. With increasing L/d_e, the measured scalings approach the predictions

the two runs with the largest L/d_e (corresponding to the two data points on the left with the smallest $\Delta_{\rm max}$). These measured scalings are different from the expected scalings ($\alpha = 3/2$ and $\nu = 1/2$) for the asymptotic regime and from the canonical Weibel theory (1).

In the same figure, we plot with the brown dash-dotted lines the analytical growth rate of the most unstable Weibel mode (top panel) and its corresponding wavenumber (bottom panel) as functions of pressure anisotropy, given by the asymptotic solution of the linear Weibel dispersion relation (Sec. 1B). This solution is obtained in the regime where an asymptotically large scale separation exists. With a large enough L/d_e (the two runs with $L/d_e = 768, 1024$), the measured growth rate and wavenumber agree well with the asymptotic solution, confirming that the primary instability producing the magnetic fields in our system is indeed the Weibel instability. As L/d_e decreases, however, the measured quantities deviate from the asymptotic solution and exhibit different scalings. We believe that this discrepancy is due to the effects of the continuous forcing under insufficient scale separation (L/d_e). With a limited L/d_e, the distribution function is already driven to a complex form when the Weibel instability becomes active (very different from a tri-Maxwellian in the asymptotic regime in an orthonormal coordinate system). In addition, during the linear Weibel stage, the assumption of a static background is no longer a good approximation if the fluid time scale $L/v_{\rm th}$ is not asymptotically large compared to the inverse growth rate $1/\gamma_B$; the effect of the shear flow in tilting the Weibel filaments is not negligible. The combination of these effects leads to different values of Weibel growth rate and wavenumber and their different scaling dependencies on Δ for limited L/d_e.

The increasing magnetic growth rate leads to super-exponential growth of magnetic energy, and thus of β^{-1} [Eq. (S18)]. When the argument of the exponential function becomes of order unity, the linear stage ends. This moment corresponds to the measured $\tau_{\rm lin}$. This is consistent with the fact that β^{-1} in runs with varying L/d_e or S_0 reaches the same value at $\tau_{\rm lin}$ (shown by the horizontal dashed lines in bottom panels of each column in Fig. S3).

The values of $\tau_{\rm lin}$ and quantities measured at $\tau_{\rm lin}$ are expected to exhibit power-law dependencies on L/d_e and S_0, according to Eq. (S19)–Eq. (S21). The exponents α and κ are obtained from our numerical results for small and moderate L/d_e (Fig. S4), and are obtained from the analytical solution at $tv_{\rm th}/L \ll 1$ for asymptotically large L/d_e [Eq. (3) and Eq. (4)]. Plugging the measured values $\alpha = 2$ and $\kappa \in \{1/2,\ 3/2\}$ into Eq. (S19)–Eq. (S21), we derive the following scalings: for the L/d_e dependence, we expect that in the post-plateau regime ($\kappa = 1/2$), $\tau_{\rm lin} \sim (L/d_e)^{-1/2}$, $\Delta_{\rm max} \sim (L/d_e)^{-1/4}$, and $\gamma_{B,\rm max} \sim (L/d_e)^{-1/2}$; in the pre-plateau regime ($\kappa = 3/2$), $\tau_{\rm lin} \sim (L/d_e)^{-1/4}$, $\Delta_{\rm max} \sim (L/d_e)^{-3/8}$, and $\gamma_{B,\rm max} \sim (L/d_e)^{-3/4}$. These latter (pre-plateau) scalings are close to those in the asymptotic regime, for which we expect $\tau_{\rm lin} \sim (L/d_e)^{-1/4}$, $\Delta_{\rm max} \sim (L/d_e)^{-1/2}$, and $\gamma_{B,\rm max} \sim (L/d_e)^{-3/4}$ (see Theory section in the main text). The above predicted scalings for the post- and pre-plateau regimes are confirmed by the numerical results shown in the left panel of Fig. S6, where the transition of scalings occurs at around $L/d_e \approx 200$, consistent with what we observe in Fig. S3.

The dependence of $\tau_{\rm lin}$, $\Delta_{\rm max}$, and $\gamma_{B,\rm max}$ on S_0 ($\hat{a}_0 \propto S_0$) is more difficult to test in our numerical results. For runs with varying S_0, the background evolution of M and Δ for the unmagnetized plasma differs and the transition between the pre- and post-plateau regimes occurs at different critical values of L/d_e. For fixed small or moderate L/d_e, Δ scales differently with time (at around $\tau_{\rm lin}$) for systems with different S_0, rendering the application of our scaling theory nontrivial. We therefore focus on the regime with asymptotically large L/d_e, where the quadratic time dependence of Δ [Eq. (4)] applies to systems with any values of S_0. In this asymptotic regime, quantities are expected to scale with S_0 as $\tau_{\rm lin} \sim S_0^{-3/8}$, $\Delta_{\rm max} \sim S_0^{1/4}$, $\gamma_{B,\rm max}/\omega_{\rm p} \sim S_0^{3/8}$ (see Theory section in the main text), shown by the red dotted lines in the right panel of Fig. S6. Three groups of runs with different values of L/d_e fixed in each case and with a parameter scan on S_0 are presented. We are not able to perform simulations deep in the asymptotic regime due to computational constraints, especially in 3D. However, it seems clear that with increasing L/d_e the measured scalings approach our asymptotic predictions.

B. Scaling laws at the saturation of Weibel instability. The saturation of Weibel instability (that we observe in the fiducial case in the main text) occurs when the produced magnetic fields become strong enough to instigate particles' gyromotion on the length scale of magnetic filaments, i.e., $k_{\rm w}\rho_e \sim 1$ (1, 4). As discussed in Sec. 2B, at saturation, ρ_e is related to the saturated magnetic field as $\rho_e \simeq \beta_{\rm sat}^{1/2} d_e$, and $k_{\rm w}$ is approximated with the inverse length scale of the magnetic field at $\tau_{\rm lin}$, determined by $\Delta_{\rm max}$: $k_{\rm w}(\tau_{\rm lin}) \simeq \Delta_{\rm max}^{\nu}/d_e$ [Eq. (S22)]. The index $\nu = 1$ is measured for the post- and pre-plateau regimes (Fig. S5, bottom panel), while $\nu = 1/2$ is expected for the asymptotic regime. The scaling $\beta_{\rm sat}^{-1} \sim \Delta_{\rm max}^2$ [Eq. (S24)] immediately follows (with $\nu = 1$), and is confirmed both in the post- and pre-plateau regimes (Fig. S7, left panel). Combined with the dependence of $\Delta_{\rm max}$ on L/d_e and S_0 [Eq. (S20) and Eq. (10)], we obtain the following predictions [Eq. (S25) and Eq. (13)]: in the post-plateau regime, $\beta_{\rm sat}^{-1} \sim (L/d_e)^{-1/2}$; in the pre-plateau regime $\beta_{\rm sat}^{-1} \sim (L/d_e)^{-3/4}$; and in the asymptotic regime, $\beta_{\rm sat}^{-1} \sim (L/d_e)^{-1/2}$. The scalings in the post- and pre-plateau regimes are confirmed by the numerical results (Fig. S7, right panel). For the same reason explained in Sec. 4A, we are only able to predict the dependence of $\beta_{\rm sat}^{-1}$ on S_0 for systems with asymptotically large L/d_e: $\beta_{\rm sat}^{-1} \sim S_0^{1/4}$ [Eq. (13)]. Although we are not able to perform simulations deep in this asymptotic regime, a clear trend is shown in Fig. S8 that the measured scalings approach the $S_0^{1/4}$ prediction with increasing L/d_e.

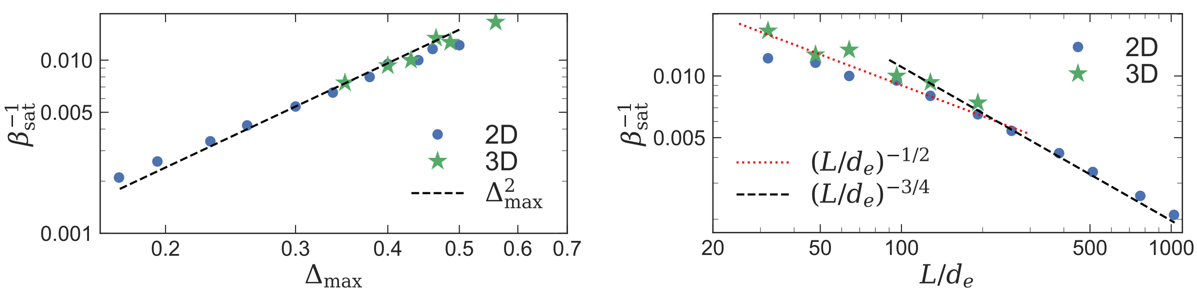

Fig. S7. Saturated inverse beta $\beta_{\rm sat}^{-1}$ versus $\Delta_{\rm max}$ (left) and versus L/d_e (right) for 2D and 3D runs with varying L/d_e and fixed $S_0 = 0.2$.

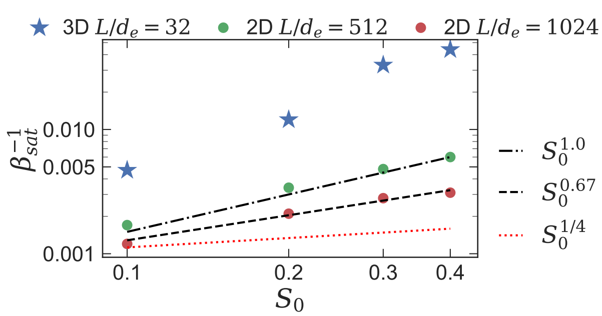

Fig. S8. Saturated inverse beta $\beta_{\rm sat}^{-1}$ versus S_0 for 2D and 3D runs with varying S_0.

The presented numerical results confirm our analytical model (Sec. 2) in the post- and pre-plateau regimes (for small and moderate L/d_e). The three exponents in the model, α, κ, and ν, are determined by the numerical results. The derived scalings [Eq. (S19)–Eq. (S21) and Eq. (S24)–Eq. (S25)], whose indices are functions of α, κ, and ν, are confirmed independently by the numerical results. The validation of our model in the post- and pre-plateau regimes gives us confidence in its predictions in the asymptotic regime, which are derived within the same framework as the other regimes. More detailed discussion about how our numerical simulations support our theory is provided in the next section.

5. Time-scale analysis

In this section, we preform a time-scale analysis to justify that, although our simulations are not in the strict asymptotic regime, their scale separation is large enough to test the modified (i.e., non-asymptotic) version of the theory; and, thus, they directly support the reasoning that underlies the asymptotic theory. We first introduce the relevant time scales in this analysis, and then explain the differences between our shear-flow setup and the conventional super-critical (to the Weibel instability) setup. After that, we compare different time scales and discuss the time-scale separation required in the asymptotic theory, in the modified theory, and that achieved in our simulations, respectively.

There are three relevant time scales: (i) the thermal crossing time L/v_{th} — this is the time scale that characterizes the evolution of the background equilibrium (the evolution of pressure anisotropy Δ) slowly driven by the imposed force; (ii) $\tau_{\mathrm{lin}}L/v_{\mathrm{th}}$ — this is the time scale for the Weibel instability to reach the end of the linear stage, i.e., the time required for the Weibel magnetic fields to reach sufficient strength to affect the evolution of the background equilibrium; and (iii) $1/\gamma_{\mathrm{B,max}}$, where $\gamma_{\mathrm{B,max}}$ is the maximum growth rate of magnetic fields that occurs at τ_{lin} (details can be found in SI) — this is the time scale for the rapid growth of magnetic fields.

We emphasize that rather than initialize a configuration that is super-critical to the Weibel instability, we instead start with a stable equilibrium and drive the system gradually towards becoming unstable to the Weibel instability. The different setups yield some differences when doing the time-scale comparison: (i) In a super-critical setup, the maximum growth rate, $\gamma_{\mathrm{B,max}}$, occurs at the beginning of the simulation, and so the time scale to reach the end of the linear stage is the same as that during which the magnetic fields grow rapidly, $\tau_{\mathrm{lin}}L/v_{\mathrm{th}} \sim 1/\gamma_{\mathrm{B,max}}$. In our driven-flow setup, initially the magnetic growth rate γ_B is small because the pressure anisotropy Δ is small. The growth of magnetic field during this initial time interval is not significant, which lengthens the time scale of the linear Weibel phase, $\tau_{\mathrm{lin}}L/v_{\mathrm{th}}$. The rapid growth of magnetic fields only occurs toward the end of the linear stage when $\gamma_{\mathrm{B,max}}$ is reached. Therefore, in our setup, $\tau_{\mathrm{lin}}L/v_{\mathrm{th}} > 1/\gamma_{\mathrm{B,max}}$. (ii) In a super-critical setup, $1/\gamma_B$ and $\tau_{\mathrm{lin}}L/v_{\mathrm{th}}$ are on the purely kinetic time scale. On the contrary, in our setup the pressure anisotropy Δ, which is set by the flow and determines γ_B in the linear phase, evolves on the fluid time scale. Therefore, $1/\gamma_B$ and $\tau_{\mathrm{lin}}L/v_{\mathrm{th}}$ are on the hybrid time scale of the kinetic time scale ($\sim 1/\omega_{\mathrm{pe}}$) and the fluid thermal crossing time ($\sim L/v_{\mathrm{th}}$).

In our asymptotic theory (described in the main text), there are two requirements for the time-scale separation. The first is about whether linear theory can be performed at all. This requires that during the time interval when magnetic fields increase rapidly ($\sim 1/\gamma_{\mathrm{B,max}}$), the change of background equilibrium (on the fluid time scale L/v_{th}) is negligible. That leads to the condition $\gamma_{B,\mathrm{max}}L/v_{\mathrm{th}} \gg 1$. Combined with the expression for the Weibel growth rate, $\gamma_B \sim \Delta^{\alpha}\omega_{\mathrm{pe}}v_{\mathrm{the}}/c$, where $\alpha = 3/2$ in the asymptotic regime and $\alpha = 2$ in our simulations, the above condition yields to $L/d_e \gg \Delta^{-\alpha}$. The values of Δ in our simulations range from 0.1 to 0.6 (Fig. S3), and so this condition of scale separation is satisfied. Therefore, the adoption of a linear theory is valid in our modified theory and when analysing simulation results.

The second requirement arises from the use of the early-time behaviour of the equilibrium distribution function. In the main text, we derived the early-time behaviour of the system by taking the Taylor expansion of the unmagnetized solution for $\epsilon \equiv tv_{\mathrm{th}}/L \ll 1$. In this limit, the equilibrium distribution is tri-Maxwellian, and yields the scalings $\Delta \sim (tv_{\mathrm{th}}/L)^2$, $\gamma_B \sim \Delta^{3/2}$, and $k_{\mathrm{w}} \sim \Delta^{1/2}/d_e$. As we mentioned in the main text, to enter the deep asymptotic regime and obtain these scalings, the short-time ($tv_{\mathrm{th}}/L \lesssim 0.1$) approximation of the unmagnetized solution needs to be valid during the growth of Weibel seed fields (at $tv_{\mathrm{th}}/L \simeq \tau_{\mathrm{lin}}$), i.e., $\tau_{\mathrm{lin}} \lesssim 0.1$. (We found that the deviation between the second-order expansion and the full solution becomes noticeable at $tv_{\mathrm{th}}/L \approx 0.1$.) The weak scaling dependence $\tau_{\mathrm{lin}} \sim (L/d_e)^{-1/4}$ then suggests that a significantly larger scale separation, $L/d_e \gtrsim 10^4$, is required to access the deep asymptotic regime. This large scale separation is not required in our modified theory, and is not achieved in our simulations. Therefore, in our modified theory in the supplementary materials, we replaced the above predictive scalings with power laws with undetermined indices, which are then measured in the simulations. Note that the satisfaction of the time-scale separation required for a linear theory ($\gamma_{B,\mathrm{max}}L/v_{\mathrm{th}} \gg 1$) in our modified theory and in the simulations justifies the use of modified power-laws: because the time interval for the growth of magnetic fields is short on the fluid time scale, we can approximate the time-dependence of slowly-evolving quantities with power-laws.

In summary, in our simulations the time scale separation is large enough to justify the linear theory, but not enough to guarantee that the equilibrium distribution remains close to a tri-Maxwellian distribution. Therefore, the simulation results can be used to test the modified theory in the non-asymptotic regime, and provide justification for the theoretical arguments described in the Theory Section in the main text.

References

1. RC Davidson, DA Hammer, I Haber, CE Wagner, Nonlinear development of electromagnetic instabilities in anisotropic plasmas. *Phys. Fluids* **15**, 317–333 (1972).
2. A Bret, Weibel, Two-Stream, Filamentation, Oblique, Bell, Buneman...Which One Grows Faster? *Astrophys. J.* **699**, 990–1003 (2009).
3. B Cerutti, GR Werner, DA Uzdensky, MC Begelman, Simulations of Particle Acceleration beyond the Classical Synchrotron Burnoff Limit in Magnetic Reconnection: An Explanation of the Crab Flares. *Astrophys. J.* **770**, 147 (2013).
4. TN Kato, Saturation mechanism of the Weibel instability in weakly magnetized plasmas. *Phys. Plasmas* **12**, 080705 (2005).